First results from the LUX dark matter experiment at the Sanford Underground Research Facility

D.S. Akerib,[2] H.M. Araújo,[4] X. Bai,[8] A.J. Bailey,[4] J. Balajthy,[16] S. Bedikian,[19] E. Bernard,[19]
A. Bernstein,[6] A. Bolozdynya,[2] A. Bradley,[2] D. Byram,[18] S.B. Cahn,[19] M.C. Carmona-Benitez,[2,14]
C. Chan,[1] J.J. Chapman,[1] A.A. Chiller,[18] C. Chiller,[18] K. Clark,[2] T. Coffey,[2] A. Currie,[4] A. Curioni,[19]
S. Dazeley,[6] L. de Viveiros,[7] A. Dobi,[16] J. Dobson,[15] E.M. Dragowsky,[2] E. Druszkiewicz,[17] B. Edwards,[19,*]
C.H. Faham,[1,5] S. Fiorucci,[1] C. Flores,[13] R.J. Gaitskell,[1] V.M. Gehman,[5] C. Ghag,[11] K.R. Gibson,[2]
M.G.D. Gilchriese,[5] C. Hall,[16] M. Hanhardt,[8,9] S.A. Hertel,[19] M. Horn,[19] D.Q. Huang,[1] M. Ihm,[12] R.G. Jacobsen,[12]
L. Kastens,[19] K. Kazkaz,[6] R. Knoche,[16] S. Kyre,[14] R. Lander,[13] N.A. Larsen,[19] C. Lee,[2] D.S. Leonard,[16]
K.T. Lesko,[5] A. Lindote,[7] M.I. Lopes,[7] A. Lyashenko,[19] D.C. Malling,[1] R. Mannino,[10] D.N. McKinsey,[19]
D.-M. Mei,[18] J. Mock,[13] M. Moongweluwan,[17] J. Morad,[13] M. Morii,[3] A.St.J. Murphy,[15] C. Nehrkorn,[14]
H. Nelson,[14] F. Neves,[7] J.A. Nikkel,[19] R.A. Ott,[13] M. Pangilinan,[1] P.D. Parker,[19] E.K. Pease,[19] K. Pech,[2]
P. Phelps,[2] L. Reichhart,[11] T. Shutt,[2] C. Silva,[7] W. Skulski,[17] C.J. Sofka,[10] V.N. Solovov,[7] P. Sorensen,[6]
T. Stiegler,[10] K. O'Sullivan,[19] T.J. Sumner,[4] R. Svoboda,[13] M. Sweany,[13] M. Szydagis,[13] D. Taylor,[9]
B. Tennyson,[19] D.R. Tiedt,[8] M. Tripathi,[13] S. Uvarov,[13] J.R. Verbus,[1] N. Walsh,[13] R. Webb,[10]
J.T. White,[10,†] D. White,[14] M.S. Witherell,[14] M. Wlasenko,[3] F.L.H. Wolfs,[17] M. Woods,[13] and C. Zhang[18]

[1] *Brown University, Dept. of Physics, 182 Hope St., Providence RI 02912, USA*
[2] *Case Western Reserve University, Dept. of Physics, 10900 Euclid Ave, Cleveland OH 44106, USA*
[3] *Harvard University, Dept. of Physics, 17 Oxford St., Cambridge MA 02138, USA*
[4] *Imperial College London, High Energy Physics, Blackett Laboratory, London SW7 2BZ, UK*
[5] *Lawrence Berkeley National Laboratory, 1 Cyclotron Rd., Berkeley CA 94720, USA*
[6] *Lawrence Livermore National Laboratory, 7000 East Ave., Livermore CA 94550, USA*
[7] *LIP-Coimbra, Department of Physics, University of Coimbra, Rua Larga, 3004-516 Coimbra, Portugal*
[8] *South Dakota School of Mines and Technology, 501 East St Joseph St., Rapid City SD 57701, USA*
[9] *South Dakota Science and Technology Authority,*
Sanford Underground Research Facility, Lead, SD 57754, USA
[10] *Texas A & M University, Dept. of Physics, College Station TX 77843, USA*
[11] *University College London, Department of Physics and Astronomy, Gower Street, London WC1E 6BT, UK*
[12] *University of California Berkeley, Department of Physics, Berkeley CA 94720, USA*
[13] *University of California Davis, Dept. of Physics, One Shields Ave., Davis CA 95616, USA*
[14] *University of California Santa Barbara, Dept. of Physics, Santa Barbara, CA, USA*
[15] *University of Edinburgh, SUPA, School of Physics and Astronomy, Edinburgh, EH9 3JZ, UK*
[16] *University of Maryland, Dept. of Physics, College Park MD 20742, USA*
[17] *University of Rochester, Dept. of Physics and Astronomy, Rochester NY 14627, USA*
[18] *University of South Dakota, Dept. of Physics, 414E Clark St., Vermillion SD 57069, USA*
[19] *Yale University, Dept. of Physics, 217 Prospect St., New Haven CT 06511, USA*
(Dated: October 30, 2013)

The Large Underground Xenon (LUX) experiment, a dual-phase xenon time-projection chamber operating at the Sanford Underground Research Facility (Lead, South Dakota), was cooled and filled in February 2013. We report results of the first WIMP search dataset, taken during the period April to August 2013, presenting the analysis of 85.3 live-days of data with a fiducial volume of 118 kg. A profile-likelihood analysis technique shows our data to be consistent with the background-only hypothesis, allowing 90% confidence limits to be set on spin-independent WIMP-nucleon elastic scattering with a minimum upper limit on the cross section of 7.6×10^{-46} cm^2 at a WIMP mass of 33 GeV/c^2. We find that the LUX data are in strong disagreement with low-mass WIMP signal interpretations of the results from several recent direct detection experiments.

Convincing evidence for the existence of particle dark matter is derived from observations of the universe on scales ranging from the galactic to the cosmological [1–

---

* Corresponding Author: blair.edwards@yale.edu
† deceased

3]. Increasingly detailed studies of the Cosmic Microwave Background anisotropies have implied the abundance of dark matter with remarkable precision [4, 5]. One favored class of dark matter candidates, the Weakly Interacting Massive Particle (WIMP), may be amenable to direct detection in laboratory experiments through its interactions with ordinary matter [6, 7]. The WIMPs

that constitute our galactic halo would scatter elastically with nuclei, generating recoil energies of several keV at a rate of less than 1 event/kg/year.

We report here the first results from the Large Underground Xenon (LUX) experiment, currently operating 4850 feet below ground (4300 m w.e.) at the Sanford Underground Research Facility (SURF) [8, 9] in Lead, South Dakota. Fluxes of cosmic-ray muons, neutrons and γ-rays at SURF have been published elsewhere [10]. Inside the cavern, a 7.6 m diameter by 6.1 m tall cylindrical water tank provides shielding to the detector. These large reductions in external radiation provide the low-background environment required for the rare event search.

The LUX detector holds 370 kg of liquid xenon, with 250 kg actively monitored in a dual-phase (liquid-gas) time-projection chamber (TPC) measuring 47 cm in diameter and 48 cm in height (cathode-to-gate) [11]. Interactions in the liquid produce prompt scintillation (S1) and ionization electrons that drift in an applied electric field [12]. Electrons are extracted into the gas, where they produce electroluminescence (S2). S1 and S2 signals are used to reconstruct the deposited energy and their ratio is used to discriminate nuclear recoils (NR) from electron recoils (ER). Light signals are detected via two arrays of 61 photomultiplier tubes (PMTs), one array above the active region in the gas and one below it in the liquid [13]. During this search, three PMTs were left unbiased, two in the top array and one in the bottom. The (x,y) position of an interaction is determined from localization of the S2 signal in the top PMT array, with the difference in time between the S1 and S2 representing event depth. S2 pulse areas measured from the bottom PMT array alone (S2$_b$) are used in later analysis, avoiding events leaking into the signal region due to uncollected S2 light from the deactivated PMTs in the top array.

Throughout the WIMP search, the xenon vessel was thermally isolated with an outer vacuum vessel providing thermal stability of $\Delta T <$0.2 K, pressure stability $\Delta P/P <$1% and liquid level variation of <0.2 mm [14]. An electric field of 181 V/cm was applied across the WIMP target region providing a measured average electron drift velocity of 1.51 ± 0.01 mm/μs. Above the drift region, a field of 6.0 kV/cm is applied to the gas (3.1 kV/cm in the liquid), producing a best-fit electron extraction efficiency of 0.65 ± 0.01.

Purification of the xenon, circulating through a hot-zirconium getter (229 kg/day), resulted in mean electron drift-lengths, before capture by electronegative impurities, between 87±9 and 134±15 cm during WIMP search.

The data acquisition (DAQ) threshold is set such that $\gtrsim$95% of all single photoelectron (phe) pulses in each PMT are recorded to disk [15, 16]. A digital trigger identifies events for further analysis, with PMTs grouped together into 16 trigger channels. The trigger requires that at least 2 of these channels have greater than 8 phe within a 2 μs window, with a trigger efficiency >99% for S2 signals above the analysis threshold of 200 phe. Every pulse of light digitized by the DAQ within ±500 μs of the trigger time (320 μs maximum drift time) was allocated to a triggered event for further analysis, ensuring that corresponding S1 and S2 pulses can always be associated. Additionally, data between triggered events are retained to verify that the detector is quiet in the period leading up to, and following, the events.

This initial dark matter search consists of 85.3 live-days of WIMP search data acquired between April 21 and August 8, 2013. The live-time calculation accounts for the DAQ dead-time (0.2%), a 1 ms trigger hold-off to prevent additional triggers following large S2 pulses (2.2%), and exclusions for periods of detector instability (0.8%).

A non-blind analysis was conducted on the 85.3 live-days of WIMP search data, where only a minimal set of data quality cuts, with high acceptance, was employed to reduce the scope for bias. The low total event rate in the center of the detector minimizes the chances of misidentifying ER background events. For this initial analysis of the first low-background operation of the instrument, both the calibration and WIMP search data were used to understand and develop analysis algorithms.

Waveforms from each PMT are summed across all channels and then searched with pulse finding algorithms to select viable signals. The identification of an S1 signal requires at least two PMTs to detect more than 0.25 phe each within 100 ns of each other. The average dark count rate for each PMT in the array is 25 Hz. An estimate of the rate of events where an accidental 2 phe dark count coincidence fakes an S1 preceding a valid S2-only event in the NR signal region is 7 nHz (0.06 events in the search dataset) [16].

Events containing exactly one S1 and one S2, representative of expected elastic scattering of WIMPs, are selected for further analysis. Additionally, we require a raw S2 pulse size greater than 200 phe ($\sim$8 extracted electrons). This excludes a small number of single-extracted-electron-type events (having poor event reconstruction) and those from the detector walls with small S2 signals (having poorly reconstructed positions). This was optimized by studying the reliability of the reconstruction algorithms in the calibration and WIMP search data.

Single scatter ER and NR acceptance was measured with dedicated tritium (β^-), AmBe, and ^{252}Cf (neutron) datasets. Simulated NR event waveforms, generated with LUXSim [17, 18], were analyzed with the complete data processing framework to validate the analysis efficiencies measured with data. S2 finding efficiency is >99% above the analysis threshold of 200 phe. The relative efficiency for NR detection is dominated by the S1 identification (shown in Fig. 1). Absolute efficiency is estimated through visual inspection of waveforms from NR calibration data to be 98%, which is in agreement with the value measured by an injection of tritiated

methane of known activity. All cuts and efficiencies combine to give an overall WIMP detection efficiency of 50% at 4.3 keV$_{nr}$ (17% at 3 keV$_{nr}$ and > 95% above 7.5 keV$_{nr}$) [39].
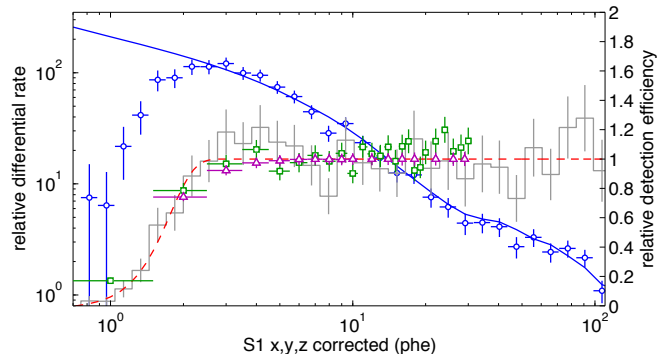

FIG. 1. Comparison of AmBe data (blue circles) with simulations (blue line), showing excellent agreement above the 2 phe threshold (left axis). The gray histogram and fitted dashed red line show the relative efficiency for detection of nuclear recoils from AmBe data (right axis). Overlaid are the ER detection efficiency from tritium data (green squares), applied to the ER background model in the profile likelihood analysis, and the efficiency from NR simulations (purple triangles), applied to the WIMP signal model.

A radial fiducial cut was placed at 18 cm (Fig. 2), defined by the position resolution for decay products from Rn daughters implanted on the detector walls. This population, primarily sub-NR band but intersecting the signal region at the lowest energies, is visible (along with other expected backgrounds) on the detector walls in Fig. 2. In height, the fiducial volume was defined by a drift time between 38 and 305 μs to reduce backgrounds from the PMT arrays and electrodes. The fiducial target mass is calculated to be 118.3 ± 6.5 kg from assessment of the homogeneous tritium data.

Periods of live-time with high rates of single electron backgrounds ($\gtrsim$ 4 extracted electrons per 1 ms event window) are removed [19–21]. The associated loss of live-time is 0.8% (measured from assessment of the full dataset, including non-triggered regions), primarily removing periods following large S2 pulses.

Extensive calibrations were acquired with internal ER sources (tritiated methane, ^{83m}Kr) and NR calibrations were performed with external neutron sources (AmBe, ^{252}Cf). The ER sources were injected into the xenon gas system and allowed to disperse uniformly, achieving a homogeneous calibration of the active region. In particular, we developed a novel tritiated-methane β^- source ($E_{max} \simeq 18$ keV) that produces events extending below 1 keV$_{ee}$, allowing ER band (Fig. 3) and detection efficiency calibrations (Fig. 1) with unprecedented accuracy; the tritiated methane is subsequently fully removed by circulating the xenon through the getter.

A ^{83m}Kr injection was performed weekly to determine the free electron lifetime and the three-dimensional cor-
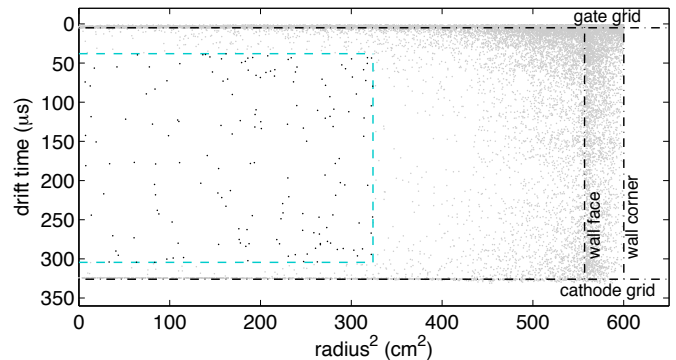

FIG. 2. Spatial distribution of all events with position-corrected S1 in the range 2-30 phe from the 85.3 live-days of WIMP search data. The cyan dashed line indicates the fiducial volume. The physical locations of the cathode and gate grids and the detector walls (where the vertical PTFE walls of the TPC form a dodecagon) are also shown.

rection functions for photon detection efficiency, which combine the effects of geometric light collection and PMT quantum efficiency (corrected S1 and S2). The 9.4 and 32.1 keV depositions [22] demonstrated the stability of the S1 and S2 signals in time, the latter confirmed with measurements of the single extracted electron response. ^{131m}Xe and ^{129m}Xe (164 and 236 keV de-excitations) afforded another internal calibration, providing a cross-check of the photon detection and electron extraction efficiencies. To model these efficiencies, we employed field- and energy-dependent absolute scintillation and ionization yields from NEST [23–25]. Applying a Gaussian fit to determine the single phe area [26], the mean S1 photon detection efficiency was determined to be 0.14±0.01, varying between 0.11 and 0.17 from the top to the bottom of the active region. This is estimated to correspond to 8.8 phe/keV$_{ee}$ (electron-equivalent energy) for 122 keV γ-rays at zero field [23]. This high photon detection efficiency (unprecedented in a xenon WIMP-search TPC) is responsible for the low threshold and good discrimination observed [27].

Detector response to ER and NR calibration sources is presented in Fig. 3. Comparison of data with simulation permits extraction of NR detection efficiency, which is in excellent agreement with that obtained using other datasets (Fig. 1). We describe the populations as a function of S1 (Fig. 3 and Fig. 4), as this provides the dominant component of detector efficiency. We also show contours of approximated constant-energy [28], calculated from a linear combination of S1 and S2 [24, 27, 29] generated by converting the measured pulse areas into original photons and electrons (given their efficiencies).

A parameterization (for S2 at a given S1) of the ER band from the high-statistics tritium calibration is used to characterize the background. In turn, the NR calibration is more challenging, partly due to the excellent self-shielding of the detector. Neutron
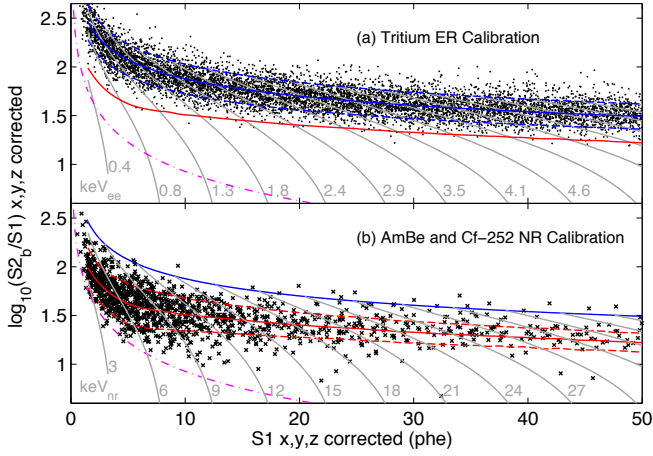
FIG. 3. Calibrations of detector response in the 118 kg fiducial volume. The ER (tritium, panel a) and NR (AmBe and ^{252}Cf, panel b) calibrations are depicted, with the means (solid line) and $\pm1.28\sigma$ from Gaussian fits to slices in S1 (dashed line). This choice of band width (indicating 10% band tails) is for presentation only. Panel a shows fits to the high statistics tritium data, with fits to simulated NR data shown in panel b, representing the parameterizations taken forward to the profile likelihood analysis. The ER plot also shows the NR band mean and vice versa. Gray contours indicate constant energies using an S1–S2 combined energy scale (same contours on each plot). The dot-dashed magenta line delineates the approximate location of the minimum S2 cut.

TABLE I. Predicted background rates in the fiducial volume (0.9–5.3 keV$_{ee}$) [31]. We show contributions from the γ-rays of detector components (including those cosmogenically activated), the time-weighted contribution of activated xenon, ^{222}Rn (best estimate 0.2 mDRUee from ^{222}Rn chain measurements) and ^{85}Kr. The errors shown are both from simulation statistics and those derived from the rate measurements of time-dependent backgrounds. 1 mDRU$_{ee}$ is 10^{-3} events/keV$_{ee}$/kg/day.

Source	Background rate, mDRU$_{ee}$
γ-rays	$1.8 \pm 0.2_{stat} \pm 0.3_{sys}$
^{127}Xe	$0.5 \pm 0.02_{stat} \pm 0.1_{sys}$
^{214}Pb	0.11–0.22 (90% C. L.)
^{85}Kr	$0.13 \pm 0.07_{sys}$
Total predicted	$2.6 \pm 0.2_{stat} \pm 0.4_{sys}$
Total observed	$3.1 \pm 0.2_{stat}$

Facility (SOLO) and the LBNL low-background counting facility [13, 26, 32]. Krypton as a mass fraction of xenon was reduced from 130 ppb in the purchased xenon to 4 ppt using gas charcoal chromatography [33].

Radiogenic backgrounds were extensively modeled using LUXSim, with approximately 80% of the low-energy γ-ray background originating from the materials in the R8778 PMTs and the rest from other construction materials. This demonstrated consistency between the observed γ-ray energy spectra and position distribution [31], and the expectations based on the screening results and the independent assay of the natural Kr concentration of 3.5 ± 1 ppt (g/g) in the xenon gas [34] where we assume an isotopic abundance of ^{85}Kr/^{nat}Kr $\sim 2 \times 10^{-11}$ [31]. Isotopes created through cosmogenic production were also considered, including measured levels of ^{60}Co in Cu components. *In situ* measurements determined additional intrinsic background levels in xenon from ^{214}Pb (from the ^{222}Rn decay chain), and cosmogenically-produced ^{127}Xe ($T_{1/2} = 36.4$ days), ^{129m}Xe ($T_{1/2} = 8.9$ days), and ^{131m}Xe ($T_{1/2} = 11.9$ days). The rate from ^{127}Xe in the WIMP search energy window is estimated to decay from 0.87 mDRU$_{ee}$ at the start of the WIMP search dataset to 0.28 mDRU$_{ee}$ at the end, with late-time background measurements being consistent with those originating primarily from the long-lived radioisotopes.

Neutron backgrounds in LUX were constrained by multiple-scatter analysis, with a conservative 90% upper C.L. placed on the number of expected neutron single scatters with S1 between 2 and 30 phe of 0.37 in the 85.3 live-day dataset, with simulations predicting a considerably lower value of 0.06 events.

We observed 160 events between 2 and 30 phe (S1) within the fiducial volume in 85.3 live-days of search data (shown in Fig. 4), with all observed events being consistent with the predicted background of electron recoils. The average discrimination (with 50% NR acceptance) for S1 from 2-30 phe is 99.6 ± 0.1%, hence 0.64 ± 0.16 events from ER leakage are expected below

calibrations therefore include systematic effects not applicable to the WIMP signal model, such as multiple-scattering events (including those where scatters occur in regions of differing field) or coincident Compton scatters from AmBe and ^{252}Cf γ-rays and (n,γ) reactions. These effects produce the dispersion observed in data, which is well modeled in our simulations (in both band mean and width, verifying the simulated energy resolution), and larger than that expected from WIMP scattering. Consequently, these data cannot be used directly to model a signal distribution. For different WIMP masses, simulated S1 and S2 distributions are obtained, accounting for their unique energy spectra.

The ratio of keV$_{ee}$ to nuclear recoil energy (keV$_{nr}$) relies on both S1 and S2, using the conservative technique presented in [29] (Lindhard with $k = 0.11$). NR data are consistent with an energy-dependent, non-monotonic reduced light yield with respect to zero field [30] with a minimum of 0.77 and a maximum of 0.82 in the range 3–25 keV$_{nr}$ [23]. This is understood to stem from additional, anti-correlated portioning into the ionization channel.

The observed ER background in the range 0.9–5.3 keV$_{ee}$ within the fiducial volume was 3.1 ± 0.2 mDRU$_{ee}$ averaged over the WIMP search dataset (summarized in Table I). Backgrounds from detector components were controlled through a material screening program at the Soudan Low-Background Counting

the NR mean, for the search dataset. The spatial distribution of the events matches that expected from the ER backgrounds in full detector simulations. We select the upper bound of 30 phe (S1) for the signal estimation analysis to avoid additional background from the 5 keV$_{ee}$ x-ray from ^{127}Xe.
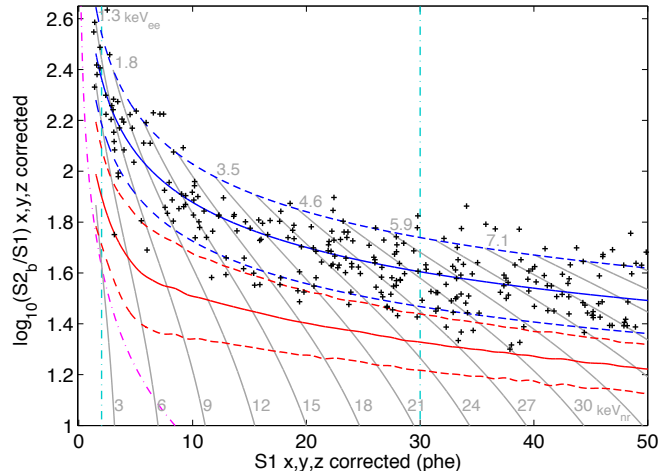

FIG. 4. The LUX WIMP signal region. Events in the 118 kg fiducial volume during the 85.3 live-day exposure are shown. Lines as shown in Fig. 3, with vertical dashed cyan lines showing the 2-30 phe range used for the signal estimation analysis.

Confidence intervals on the spin-independent WIMP-nucleon cross section are set using a profile likelihood ratio (PLR) test statistic [35], exploiting the separation of signal and background distributions in four physical quantities: radius, depth, light (S1), and charge (S2). The fit is made over the parameter of interest plus three Gaussian-constrained nuisance parameters which encode uncertainty in the rates of ^{127}Xe, γ-rays from internal components and the combination of ^{214}Pb and ^{85}Kr. The distributions, in the observed quantities, of the four model components are as described above and do not vary in the fit: with the non-uniform spatial distributions of γ-ray backgrounds and x-ray lines from ^{127}Xe obtained from energy-deposition simulations [31].

The energy spectrum of WIMP-nucleus recoils is modeled using a standard isothermal Maxwellian velocity distribution [36], with $v_0 = 220$ km/s; $v_{esc} = 544$ km/s; $\rho_0 = 0.3$ GeV/c^3; average Earth velocity of 245 km s^{-1}, and Helm form factor [37, 38]. We conservatively model no signal below 3.0 keV$_{nr}$ (the lowest energy for which direct NR yield measurements exist [30, 40]). We do not profile the uncertainties in NR yield, assuming a model which provides excellent agreement with LUX data (Fig. 1 and [39]), in addition to being conservative compared to past works [23]. We also do not account for uncertainties in astrophysical parameters, which are beyond the scope of this work. Signal models in S1 and S2 are obtained for each WIMP mass from full simulations.
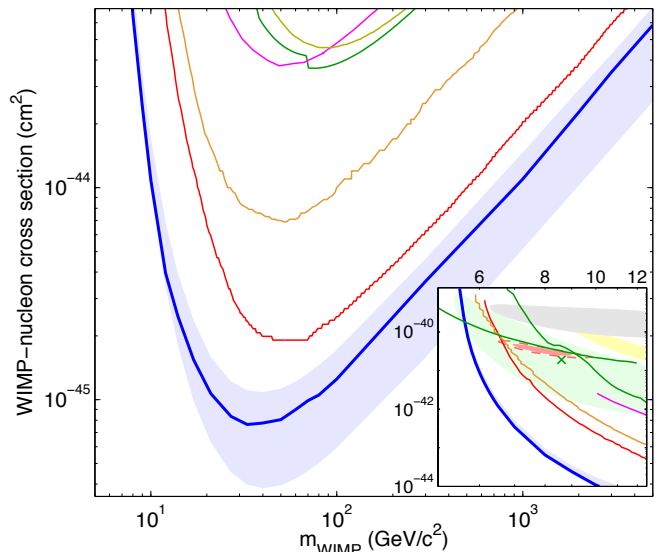

FIG. 5. The LUX 90% confidence limit on the spin-independent elastic WIMP-nucleon cross section (blue), together with the $\pm 1\sigma$ variation from repeated trials, where trials fluctuating below the expected number of events for zero BG are forced to 2.3 (blue shaded). We also show Edelweiss II [41] (dark yellow line), CDMS II [42] (green line), ZEPLIN-III [43] (magenta line) and XENON100 100 live-day [44] (orange line), and 225 live-day [45] (red line) results. The inset (same axis units) also shows the regions measured from annual modulation in CoGeNT [46] (light red, shaded), along with exclusion limits from low threshold re-analysis of CDMS II data [47] (upper green line), 95% allowed region from CDMS II silicon detectors [48] (green shaded) and centroid (green x), 90% allowed region from CRESST II [49] (yellow shaded) and DAMA/LIBRA allowed region [50] interpreted by [51] (grey shaded).

The observed PLR for zero signal is entirely consistent with its simulated distribution, giving a p-value for the background-only hypothesis of 0.35. The 90% C. L. upper limit on the number of expected signal events ranges, over WIMP masses, from 2.4 to 5.3. A variation of one standard deviation in detection efficiency shifts the limit by an average of only 5%. The systematic uncertainty in the position of the NR band was estimated by averaging the difference between the centroids of simulated and observed AmBe data in log(S2$_b$/S1). This yielded an uncertainty of 0.044 in the centroid, which propagates to a maximum uncertainty of 25% in the high mass limit.

The 90% upper C. L. cross sections for spin-independent WIMP models are thus shown in Fig. 5 with a minimum cross section of 7.6×10^{-46} cm^2 for a WIMP mass of 33 GeV/c^2. This represents a significant improvement over the sensitivities of earlier searches [42, 43, 45, 46]. The low energy threshold of LUX permits direct testing of low mass WIMP hypotheses where there are potential hints of signal [42, 46, 49, 50]. These results do not support such hypotheses based

on spin-independent isospin-invariant WIMP-nucleon couplings and conventional astrophysical assumptions for the WIMP halo, even when using a conservative interpretation of the existing low-energy nuclear recoil calibration data for xenon detectors.

LUX will continue operations at SURF during 2014 and 2015. Further engineering and calibration studies will establish the optimal parameters for detector operations, with potential improvements in applied electric fields, increased calibration statistics, decaying backgrounds and an instrumented water tank veto further enhancing the sensitivity of the experiment. Subsequently, we will complete the ultimate goal of conducting a blinded 300 live-day WIMP search further improving sensitivity to explore significant new regions of WIMP parameter space.

Finally, we would like to acknowledge the major contribution to the design, construction and operation of LUX by Professor James White. He was a founding member of the collaboration, but died this year shortly before our results were published. He will be greatly missed by us all.

[1] G. R. Blumenthal, S. Faber, J. R. Primack and M. J. Rees, Nature **311**, 517 (1984).
[2] M. Davis, G. Efstathiou, C. S. Frenk and S. D. M. White, Astrophys. J. **292**, 371 (1985).
[3] D. Clowe, M. Bradac, A. H. Gonzalez, M. Markevitch, S. W. Randell, C. Jones and D. Zaritsky, Astrophys. J. **648**, 109 (2006).
[4] C. L. Bennett, *et al.*, ApJS, **208** (2013) 20B.
[5] P. Ade, *et al.* (Planck Collaboration), arXiv:1303.5076 [astro-ph.CO].
[6] M. W. Goodman and E. Witten, Phys. Rev. D**31**, 3059 (1985).
[7] J. L. Feng, Ann. Rev. Astron. Astrophys. **48**, 495 (2010).
[8] K. T. Lesko, *et al.*, Deep Underground Science and Engineering Laboratory, Preliminary Design Report, arXiv:1108.0959 [hep-ex].
[9] K. T. Lesko, Eur. Phys. J. Plus **127**, 107 (2012).
[10] D.-M. Mei, C. Zhang, K. Thomas and F. Gray, Astroparticle Physics **34** (2010) 33-39; and F. E. Gray, C. Ruybal, J. Totushek, D.-M. Mei, K. Thomas, C. Zhang, Nucl. Inst. and Methods **A638**, 63 (2011).
[11] D. S. Akerib, *et al.*, (LUX Collaboration), Nuc. Inst. and Methods **A704**, 111 (2013).
[12] V. Chepel, H. Araujo, JINST **8** (2013) R04001.
[13] D. S. Akerib, *et al.*, (LUX Collaboration), Nuc. Inst. and Methods **A703**, 1 (2013).
[14] P. Phelps, Ph.D thesis (in preparation), Case Western Reserve University, 2014.
[15] D. S. Akerib, *et al.*, (LUX Collaboration), Nuc. Inst. and Methods in Physics Research **A668**, 1 (2012).
[16] J. J. Chapman, Ph.D thesis (in preparation), Brown University, 2014.
[17] D. S. Akerib, *et al.* (LUX Collab.), Nuc. Inst. and Methods **A675**, 63 (2011).
[18] J. Mock, *et al.*, arXiv:1310.1117 (2013), submitted to JINST.
[19] B. Edwards *et al.*, Astroparticle Physics, **30** (2008) 471.
[20] J. Angle *et al.*, Phys. Rev. Lett. **107**, 051301 (2011).
[21] E. Santos *et al.*, J. High Energy Phys. (2011) 115.
[22] L. W. Kastens, S. B. Cahn, A. Manzur, D. N. McKinsey, Phys. Rev. C **80**, 045809 (2009); and A. Manalaysay, *et al.*, Rev. Sci. Instrum. **81**, 073303 (2010).
[23] M. Szydagis, *et al.*, JINST **8** (2013) C10003.
[24] M. Szydagis, *et al.*, JINST **6** (2011) P10002.
[25] L. Baudis, *et al.*, Phys. Rev. D **87**, 115015 (2013); and E. Aprile, *et al.*, Phys. Rev. D **86** (2012) 112004.

[26] C. H. Faham, Ph.D thesis, Brown University, 2013.

[27] C. E. Dahl, Ph.D. thesis, Princeton University, 2009.

[28] P. Sorensen, Phys. Rev. D **86**, 101301 (2012).

[29] P. Sorensen, C. E. Dahl, Phys. Rev. D **83**, 063501 (2011).

[30] G. Plante *et al.*, Phys. Rev. C **84**, 045805 (2011).

[31] LUX Backgrounds Paper, *in preparation*.

[32] D. S. Akerib, *et al.* (LUX Collab.), arXiv:1112.1376.

[33] A. I. Bolozdynya, *et al.*, Nucl. Inst. Meth. A **579** (2007) 50; D. S. Akerib, *et al.* (LUX Collab.), *in preparation*.

[34] A. Dobi, *et al.*, Nucl. Inst. Meth. A **665** (2011) 1.

[35] G. Cowan, *et al.*, Eur. Phys. J. **C71** (2011) 1554.

[36] C. Savage, K. Freese, and P. Gondolo, Phys. Rev. D **74**, 043531(2006). This paper improves upon the Lewin-Smith calculation by properly including the effect of the solar-system velocity on the cut-off at high WIMP velocity.

[37] R. Helm, Phys. Rev. **104** (1966) 1466.

[38] J. D. Lewin, P. F. Smith, Astroparticle Physics, **6** (1996) 87-112.

[39] Appendix A – Supplementary materials for this paper, submitted to Phys. Rev. Lett.

[40] A. Manzur, *et al.*, Phys. Rev. C **81** 025808 (2010).

[41] E. Armengaud *et al.*, Phys. Lett. B **702** (2011) 329-335.

[42] Z. Ahmed, *et al.*, Science **327**, 1619 (2010); and R. Agnese *et al.*, arXiv:0912.3592 [hep-ex].

[43] D. Akimov, *et al.*, Phys. Lett. B **709**, 14 (2012).

[44] E. Aprile, *et al.*, Phys. Rev. Lett. **107**, 131302 (2011).

[45] E. Aprile, *et al.*, Phys. Rev. Lett. **109**, 181301 (2012).

[46] C. E. Aalseth, *et al.*, Phys. Rev. D **88**, 012002 (2013).

[47] Z. Ahmed, *et al.*, Phys. Rev. Lett. **106**, 131302 (2011).

[48] R. Agnese, *et al.*, submitted to: Phys. Rev. Lett. (2013).

[49] G. Angloher, *et al.*, Eur.Phys.J. **C72** (2012) 1971.

[50] R. Bernabei, *et al.*, Eur.Phys.J. **C56** (2008) 333.

[51] C. Savage, *et al.*, JCAP **0904** (2009) 010.

Appendix A: Supplementary Material

This appendix contains supplementary material in support of the above paper. We show details of:

- Figure 6 – the matching of AmBe MC simulations and data in the ionization channel.

- Table II – the number of events in the WIMP search dataset, following the application of each set of cuts.

- Figures 7 and 8 – the observed and expected background energy spectra at high and low energy.

- Figure 9 – the detection efficiencies as a function of nuclear recoil energy.

- Figure 10 – the discrimination/leakage fraction of ER to NR signals as a function of S1.
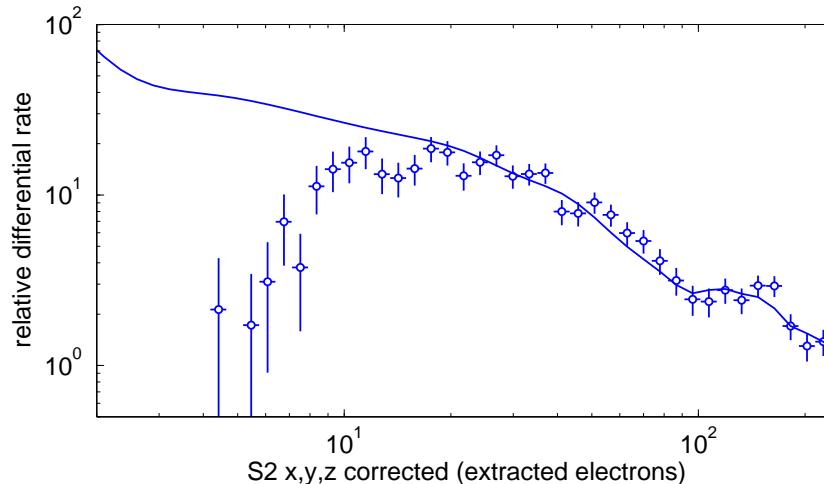

FIG. 6. Comparison of Am-Be data (blue circles) to Monte Carlo simulations (blue line) in terms of the S2 signal for single nuclear recoil scatter events. This is the complementary plot for Fig. 1 in [1]. The experimental data shows good agreement with the simulations above ~ 20 extracted electrons, at lower energies the data is affected by the S1 detection efficiency. This demonstrates that not only the light yield but also the charge yield data is well described by the NEST simulation, used in the PLR to model signal as a function of WIMP mass.

Cut	Events Remaining
all triggers	83,673,413
detector stability	82,918,902
single scatter	6,585,686
S1 energy ($2 - 30$ phe)	26,824
S2 energy ($200 - 3300$ phe)	20,989
single electron background	19,796
fiducial volume	160

TABLE II. Number of events remaining after each analysis cut. All of these cuts are commutative, the order indicating the order in which the cuts are applied in the analysis. Detector stability cuts remove periods of live-time when the liquid level, gas pressure, or grid voltages were out of nominal ranges. The single scatter cut keeps only events containing one S1 and one S2 pulse, representative of expected elastic scattering of WIMPs. S1 and S2 energy cuts keep only those events in the WIMP search energy range. Additionally, the S2 energy threshold of 200 phe removes single-extracted-electron-type events and events with unreliable position reconstruction. Periods of live-time with high rates of single electron backgrounds are then removed. The fiducial volume cut selects only those events with reconstructed radius less than 18 cm, and electron drift time between 38 and 305 μs. The final number of events in the WIMP search profile likelihood is 160. A more detailed description of the cuts is provided in the above paper.
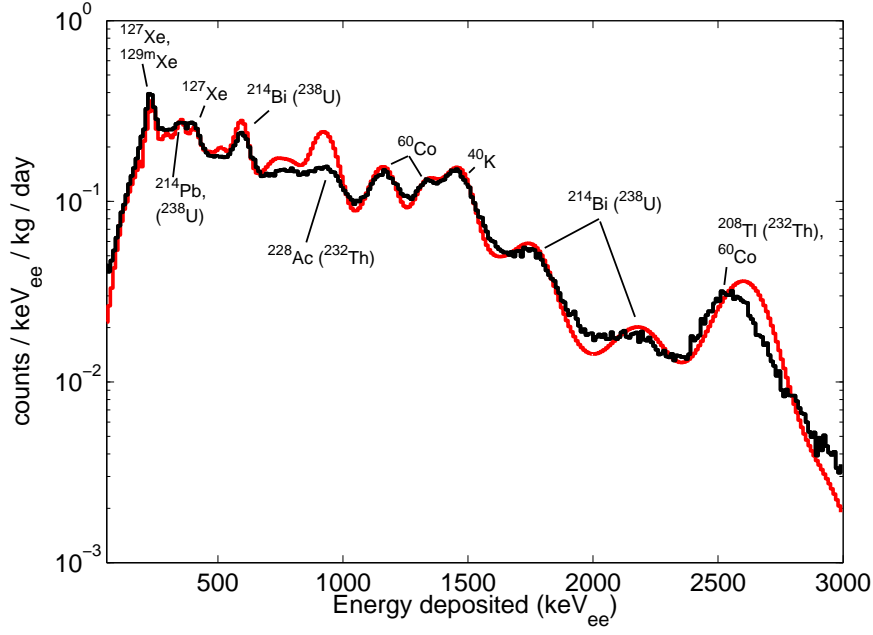
FIG. 7. Measured gamma energy spectrum in the 270 kg LUX drift region (black). Measured spectrum includes both single and multiple scatter events, and is reconstructed from combined S1 and S2 signals. No fiducial cuts are used. The high-energy spectrum from simulation (red) is also shown based on best-fit parameters with measured data. Simulations feature gammas generated from ^{238}U, ^{232}Th, ^{40}K, and ^{60}Co decays, spread over the top, bottom, and side construction materials adjoining the active region, as well as activated xenon evenly distributed in the bulk. The best-fit spectrum was matched to data over 13 slices in depth, for energies >500 keVee. [31]
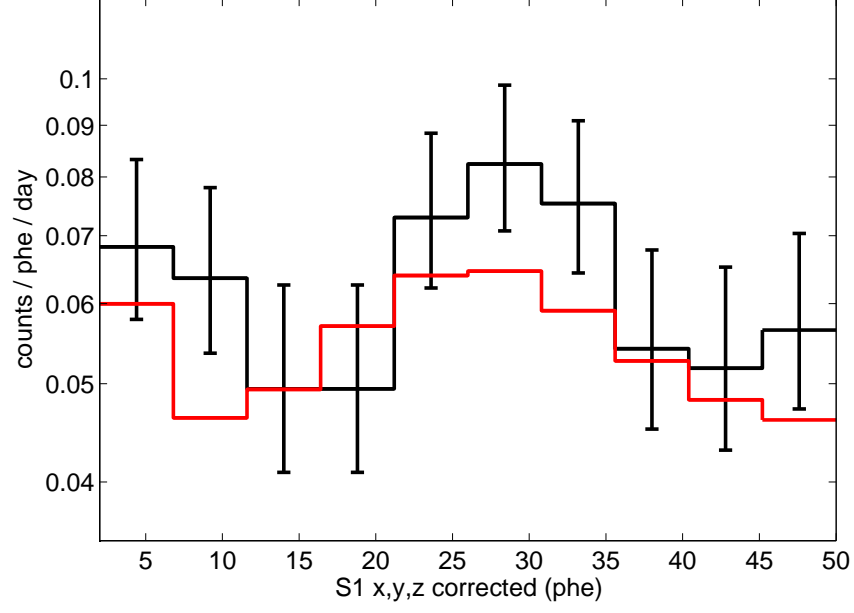
FIG. 8. S1 distribution of low-energy backgrounds within the 118 kg WIMP search fiducial volume, ranging from 2–50 phe (black). Data shown includes all WIMP search selection cuts. Simulation predictions based on models of gamma, ^{127}Xe, ^{214}Pb, and ^{85}Kr low-energy background contributions are shown for comparison (red). Gamma, ^{127}Xe and ^{214}Pb low-energy model predictions are extrapolated from independent high-energy measurements. ^{85}Kr rates are estimated based on the direct measurement of the Kr content of LUX xenon, with an assumed 2×10^{-11} ^{85}Kr / nat Kr. Count expectations are based on an 85 live-day exposure. [31]
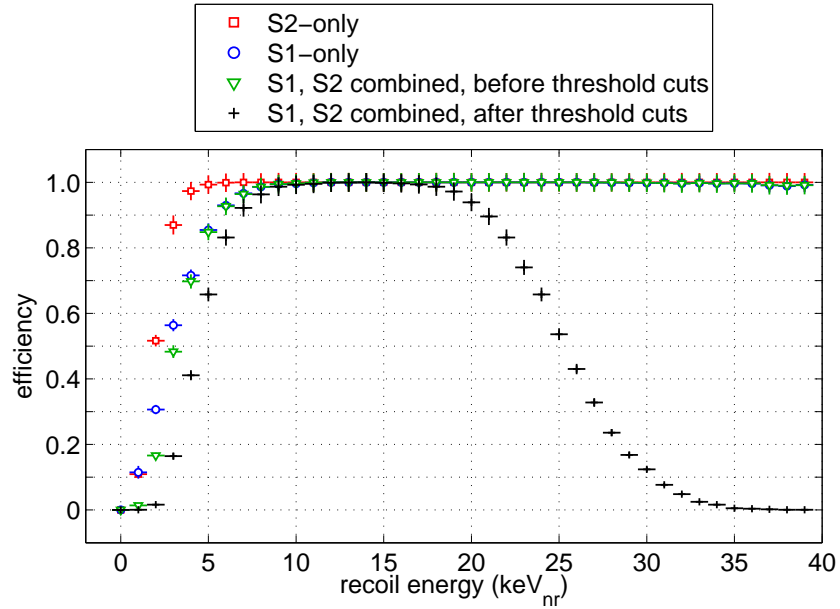

FIG. 9. WIMP detection efficiency as a function of nuclear recoil energy for events with a corrected S1 between 2 and 30 phe and a S2 signal greater than 200 phe (black +). This efficiency is used directly in the profile likelihood analysis. In addition, we show the efficiency for individually detecting an S2 (red squares) or S1 (blue circles) signal, respectively, without the application of any analysis thresholds. The detection efficiency for single scatter events (again applying no threshold cuts), shown by the green triangles, clearly demonstrate the dominant impact of the S1-only efficiency.
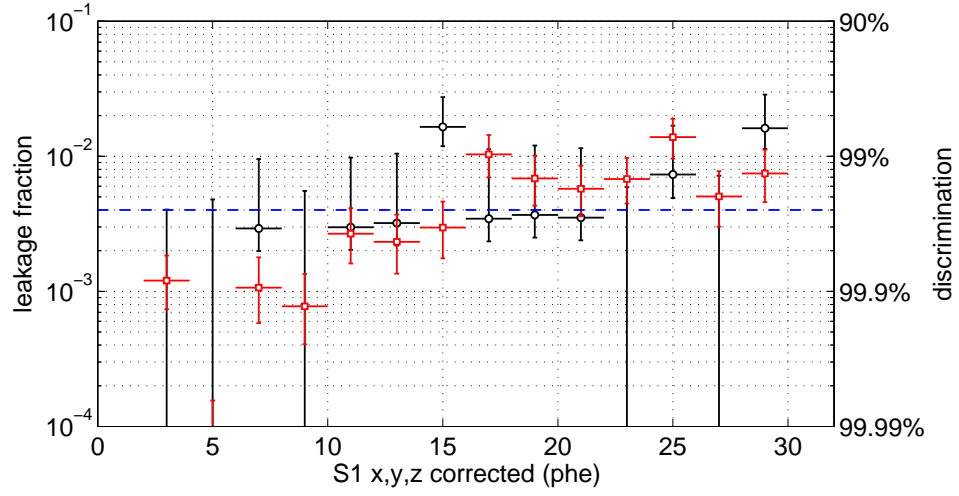
FIG. 10. Plot showing the leakage fraction (discrimination level) between electron and nuclear recoil populations, with 50% nuclear recoil acceptance (as calculated from flat-in-energy NR simulations), measured with the high-statistics tritium data. We show the leakage from counting events in the dataset (black circles) and from projections of Gaussian fits to the electron recoil population (red squares). An upper limit is shown for S1 bins without events. The blue dashed line indicates the total leakage fraction, 0.004, in the S1 range 2-30 phe. The leakage fraction is not used directly in the estimation of the WIMP signal.